

ISSN: (Print) (Online) Journal homepage: <https://www.tandfonline.com/loi/gmcl20>


Performances analysis of heterojunction solar cells through integration of hydrogenated nanocrystalline silicon bilayer by using numerical study

Dadan Hamdani, Yoyok Cahyono, Gatut Yudoyono & Darminto Darminto

To cite this article: Dadan Hamdani, Yoyok Cahyono, Gatut Yudoyono & Darminto Darminto (2021) Performances analysis of heterojunction solar cells through integration of hydrogenated nanocrystalline silicon bilayer by using numerical study, Molecular Crystals and Liquid Crystals, 725:1, 91-110, DOI: [10.1080/15421406.2021.1922226](https://doi.org/10.1080/15421406.2021.1922226)

To link to this article: <https://doi.org/10.1080/15421406.2021.1922226>

 View supplementary material [↗](#)

 Published online: 26 Jun 2021.

 Submit your article to this journal [↗](#)




 Article views: 42

 View related articles [↗](#)

 View Crossmark data [↗](#)



Performances analysis of heterojunction solar cells through integration of hydrogenated nanocrystalline silicon bilayer by using numerical study

Dadan Hamdani^{a,b} , Yoyok Cahyono^a, Gatut Yudoyono^a , and Darminto Darminto^{a,c} 

^aAdvanced Materials Research Group, Department of Physics, Institut Teknologi Sepuluh Nopember, Surabaya, Indonesia; ^bPhysics Study Program, FMIPA, Mulawarman University, Samarinda, Indonesia; ^cCenter of Excellence in Automotive Control and System, Institut Teknologi Sepuluh Nopember, Surabaya, Indonesia

ABSTRACT

This study was conducted to simulate a pin-type thin film solar cell by integrating nc-Si:H as p-window and buffer layers. The structures proposed to investigated are ITO/(p)nc-Si:H/(i)a-Si:H/(n)a-Si:H/Ag and ITO/(p)nc-Si:H/(p')nc-Si:H(buff)/(i)a-Si:H/(n)a-Si:H/Ag simulated with the AFORS-HET simulator. In an effort to improve the electrical and optical properties of the heterojunction solar cell, the dopant concentration for the p-window and n-layers, the absorber bandgap, and the absorber thickness were optimized. The result showed that the E_{ff} of p-p'-i-n is 9.60% ($V_{OC} = 936.6$ mV, $J_{SC} = 13.86$ mA/cm², $FF = 0.738$) were obtained when values of N_a , N_d , absorber bandgap, and absorber thickness parameters are 1.0×10^{17} particles/cm³, 1.0×10^{19} particles/cm³, 1.80 eV, and 600 nm, respectively.


KEYWORDS

AFORS-HET; buffer layer; nc-Si:H; p/i interface; thin film solar cells

1. Introduction

Solar cells' ability to convert sunlight into electrical energy is one of the strategies undertaken to overcome the current world energy crisis. The development of crystalline silicon (c-Si) solar cell technology based on an economic perspective is not fully commercially viable on a broader scale. This is due to the expensive investment cost associated with installing the PV system, as well as the higher costs of the fabrication process [1]. Thin film-based solar cells, such as the hydrogenated amorphous silicon (a-Si:H) are one of the solutions developed to overcome this problem. It acts as an alternative for advanced PV technology compared to crystalline silicon because of its flexibility in optical gap engineering, nontoxic nature, low cost, processing at a lower temperature, simple stages of the fabrication process, and the ability to be produced on a large scale [2]. However, despite being economically feasible with many exciting properties, a-Si:H

CONTACT Darminto Darminto  darminto@physics.its.ac.id  Advanced Materials Research Group, Department of Physics, Institut Teknologi Sepuluh Nopember, Surabaya 60111, Indonesia; Dadan Hamdani  dadan.hamdani16@mhs.physics.its.ac.id  Advanced Materials Research Group, Department of Physics, Institut Teknologi Sepuluh Nopember, Surabaya 60111, Indonesia

 Supplemental data for this article is available online at <https://doi.org/10.1080/15421406.2021.1922226>.

based solar cell offers low conversion efficiency due to light-induced degradation (LID) effect (Staebler-Wronski effect) [3]. Therefore, one of the efforts made to improve its performance is by adding low concentrations of phosphine doping into the (i) a-Si:H layer, which increases the conversion efficiency of solar cells to 8.85% [4]. According to the Advanced Industrial Science and Technology (AIST) Japan, the efficiency of amorphous single junction solar cell is approximately 10.2% [5]. Furthermore, the low efficiency of a-Si:H thin solar cells can be increased by adding other materials with a wide optical bandgap, such as a-SiC:H, and nc-Si:H, which are used as p-window layer materials to harvest a wider range of spectrum sunlight and increase the conductivity in order to improve the built-in electrical potential and minimize the effect of series resistance [6]. Conversely, the presence of the p/i interface is a heterojunction that causes a bandgap offset on the defect rich region (DRR). The offset at the valence band forms a high barrier that inhibits photogenerated holes from the absorber to the p-window layers [7]. Therefore, to enhance the solar cell's conversion efficiency, it is essential to utilize high-quality p-window and intrinsic layers. Furthermore, from the standpoint of the cell device, the p/i interface also plays a crucial role in decreasing the mismatch bandgap and minimizing charge carrier recombination. The recombination or trap centers at the p/i interface appear from the internal electric field distribution due to the localized state [8]. The quality of the p/i interface on a-Si:H-based solar cells can be meliorated by incorporated hydrogenated amorphous silicon carbide (a-SiC:H) layer as a p-window or as additional layers (buffer) to increase V_{OC} [9]. The pin structure with hydrogenated nanocrystalline silicon (nc-Si:H) consisting of boron-doped as the p-window layer with band gap range of 1.9-2.1 eV have been used for thin-film solar cell applications [10]. The nc-Si:H is a two-phase-mixed material with nanometre-sized crystals planted in an amorphous silicon matrix [11]. Furthermore, a solar cell material with wider bandgap is used to degrade the hot-carrier loss and improve the built-in potential (V_{bi}), in order to achieve higher V_{OC} , thereby increasing the solar cell efficiency. The crystalline's existence in an amorphous silicon matrix confirms the stability of the solar cells when exposed to light [12].

On the other hand, Numerical simulation to model, which simulates solar cells' performance, is one of the solutions used to analyze the best structure for solar cell to solve the problems associated with complexity fabrication costs and processing time. The use of numerical simulation in solar cell research helps to test the validity of the proposed physical structure, the solar cells performances, and output adjustment modeling of the experimental results [13]. Numerical simulation is carried out using AMPS-1D (Analysis of Microelectronic and Photonic Structures) [14, 15], AFORS-HET (Automat For Simulation HETero-structure) [16–18], TCAD (Technology Computer Aided Design) [19, 20], etc. It provides an accurate and simple way to evaluate the effect of various parameters in the solar cell fabrication process, such as the quality of amorphous materials, emitter doping, intrinsic layer thickness a-Si:H, etc. [21].

This study demonstrated and simulated the p-i-n solar cell-based a-Si:H to optimize parameters with a detailed understanding of insights in physics to overcome the lower conversion efficiency issues in thin-film solar cells fabrication [22]. The proposed structure consists of a wide bandgap nc-Si:H as p-window and buffer layer, namely, p-i-n (without buffer) and p-p'-i-n (with buffer) configurations, numerically investigated

using AFORS-HET and compared with the simulated PV characteristics of the other reference solar cell based on a-Si:H window layer and interrelated material parameters for the proposed structures taken from other studies [23, 24].

2. Solar cell structures and simulation details

Homojunction and heterojunction simulation models such as AFORS-HET (Automat FOR Simulation of Heterojunction) are needed to understand solar cells' physical processes. A detailed simulation is obtained by simultaneously determining the electrons and holes using Poisson's and continuity equations [25]

$$\frac{\varepsilon_o \varepsilon_r(x)}{q} \frac{\partial \phi^2(x, t)}{\partial x^2} = p(x, t) - n(x, t) + Nd(x) - Na(x) + \sum_{trap} \rho_{trap}(x, t) \quad (1)$$

$$-\frac{1}{q} \left(\frac{\partial J_n(x, t)}{\partial x} \right) = G_n(x, t) + R_n(x, t) - \frac{\partial n(x, t)}{\partial t} \quad (2)$$

$$+\frac{1}{q} \left(\frac{\partial J_p(x, t)}{\partial x} \right) = G_p(x, t) - R_p(x, t) - \frac{\partial p(x, t)}{\partial t} \quad (3)$$

where $\varepsilon_o \varepsilon_r$ is the absolute dielectric constant, $\phi(x, t)$ is the electric potential, q is the electron charge, $n(x, t)$ and $p(x, t)$ are electrons and holes densities, $Nd(x)$ and $Na(x)$ are the doping densities (donor and acceptor) at fixed position x , ρ_{trap} is the defect density of charge defect specifying the number of traps at any energy position E within band gap (the defect type can be empty or occupied with a single or double electron), $G(x, t)$ denotes the generation rate for carriers, and $R(x, t)$ is the recombination rate.

The optical super-band gap generation rate is equal for electrons and holes due to photon absorption within bulk semiconductor, where $G_n(x, t) = G_p(x, t) = G(x, t)$ [25]

$$G(x, t) = \int_{\lambda_{min}}^{\lambda_{max}} d\lambda \Phi_0(\lambda, t) R(\lambda) A(\lambda) \alpha_x(\lambda) \exp \left[\frac{-\alpha_x(\lambda)x}{\cos(\gamma)} \right] \quad (4)$$

where λ_{min} , λ_{max} are the minimum and maximum wavelengths for the loaded spectral range of the incoming spectral photon flux, $\Phi_0(\lambda, t)R(\lambda)A(\lambda)$ is photon flux impinging on window layer, $\alpha_x(\lambda)$ is photon absorption ($\alpha_x(\lambda) = 4\pi k(\lambda)/\lambda$), and γ is the light travels through the layer stack.

The trapping and recombination mechanism for amorphous silicon from equations (2) and (3) can be replaced by total recombination $R_T(x)$, which is the sum of recombination rates through the single level trap, through the tail, and dangling bond states (D^+ , D^0 , D^-) [7]

$$R_T(x) = R_{RSH}(x) + R_{TD}(x) + R_{DB}(x) \quad (5)$$

where $R_{RSH}(x)$ is the recombination rate through single level step, $R_{TD}(x)$ is the recombination rate of tail states, and $R_{DB}(x)$ is the recombination rate of dangling bond states.

The number of defects states $N_{trap}(E)$ can be expressed as the density of states (DOS) for the localized states as well as the valence and conduction band tail states and Gaussian distributed within the bandgap [25]

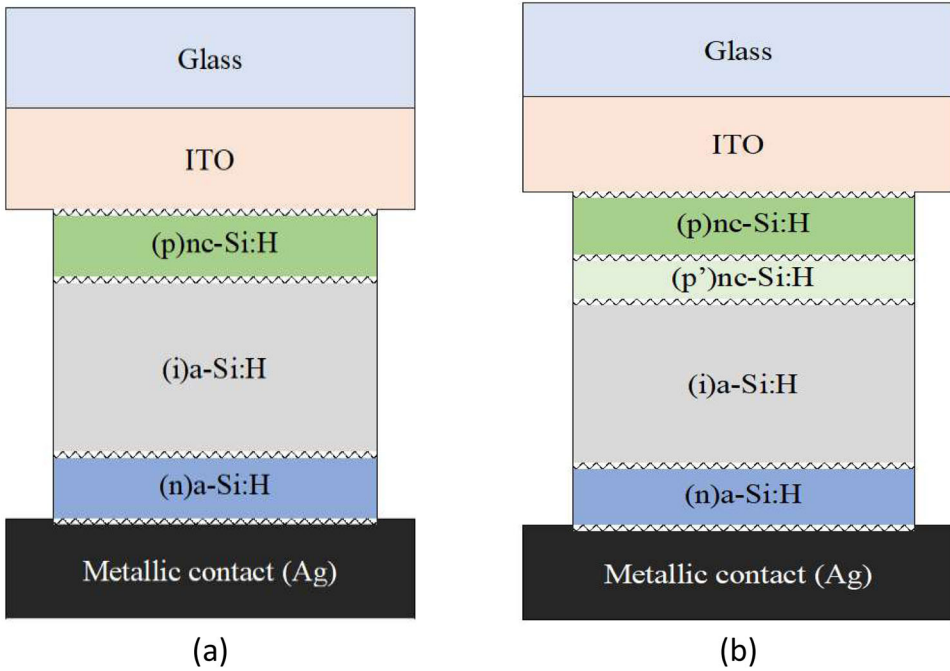


Figure 1. The pin-type heterojunction solar cells: (a) structure without buffer layer (pin); (b) structure with buffer layer (pp'in).

$$N_{trap}(E) = N_{trap}^{C,tail} \exp \left[- \left(\frac{E_C - E}{E_{trap}^{C,tail}} \right) \right] \quad (6)$$

$$N_{trap}(E) = N_{trap}^{V,tail} \exp \left[- \left(\frac{E_C - E}{E_{trap}^{V,tail}} \right) \right] \quad (7)$$

$$N_{trap}(E) = \frac{N_{trap}^{db}}{\sigma_{trap}^{db} \sqrt{2}} \exp \left(- \frac{1}{2} \left(\frac{E - E_{trap}^{db}}{\sigma_A^{db}} \right)^2 \right) \quad (8)$$

where $N_{trap}^{C,tail}$ and $N_{trap}^{V,tail}$ are the tail state density per energy range at the conduction and valence bands, $E_{trap}^{C,tail}$ and $E_{trap}^{V,tail}$ are characteristic decay energy (Urbach energy) of the conduction and valence bands, E_V and E_C are the valence and conduction band energies, N_{trap}^{db} is total dangling bond state density, E_{trap}^{db} is specific energy of Gaussian dangling bond peak, and σ_{trap}^{db} is standard deviation of the Gaussian dangling bond distribution.

Fig. 1(a) analyzes the two solar cells structures for simulation i.e. structure without buffer, namely glass/TCO(ITO)/(p)nc-Si:H(15 nm)/(i)a-Si:H(300 nm)/(n)a-Si:H(25 nm)/Ag, realized in this research group [16]. Meanwhile, Fig. 1 (b) analyzes the structure with buffer layer, namely glass/TCO(ITO)/(p)nc-Si:H(15 nm)/(p')nc-Si:H(10 nm)/(i)a-Si:H(300 nm)/(n)a-Si:H(25 nm)/Ag adopted from [17]. According to Park, et al, 2013, the abrupt band gap discontinuity and mismatch originating from the hydrogenated silicon alloy/nc-Si:H ($E_g \approx 2.0$ eV)/a-Si:H(i) ($E_g \approx 1.72$ eV) heterojunction, a thin highly

Table 1. Some input parameters for AFORS-HET simulator.

Parameters	(p)nc-Si:H	(p')nc-Si:H (buffer)	(i)a-Si:H (IL)	(i)a-Si:H	(n)a-Si:H
Thickness (nm)	15	10	2	300	25
Dielectric constant	11.9	11.9	11.9	11.9	11.9
Electron affinity (eV)	3.70	3.70	3.8	3.8	3.8
Band gap (eV)	2.0	1.88	1.72	1.72	1.72
Effective cond. band density (cm ⁻³)	2.8×10^{19}	2.8×10^{19}	2.5×10^{20}	2.5×10^{20}	2.5×10^{20}
Effective val. band density (cm ⁻³)	1.04×10^{19}	1.04×10^{19}	2.5×10^{20}	2.5×10^{20}	2.5×10^{20}
Acceptor concentration, Na (cm ⁻³)	3.0×10^{18}	1.0×10^{16}	0	0	0
Donor concentration, Nd (cm ⁻³)	0	0	0	0	1.0×10^{19}
Electron mobility (cm ² V ⁻¹ s ⁻¹)	2.0	2.0	20	20	10
Hole mobility (cm ² V ⁻¹ s ⁻¹)	0.2	0.2	2	2	1
Thermal velocity of electron (cms ⁻¹)	1.0×10^7	1.0×10^7	1.0×10^7	1.0×10^7	1.0×10^7
Thermal velocity of hole (cms ⁻¹)	1.0×10^7	1.0×10^7	1.0×10^7	1.0×10^7	1.0×10^7
Layer density (gcm ⁻³)	2.328	2.328	2.328	2.328	2.328
Defect density at conduction (valence) band edge (cm ⁻³ eV ⁻¹)	2.0×10^{20}	2.0×10^{20}	2.0×10^{21}	2.0×10^{21}	2.0×10^{21}
Urbach energy for conduction (valence) band tail (eV)	0.01(0.02)	0.01(0.02)	0.03(0.07)	0.03(0.05)	0.03(0.05)
Capture cross section σ_e (σ_h) for conduction band tail (cm ²)	1.0×10^{-17}	1.0×10^{-17}	4.0×10^{-13}	1.0×10^{-17}	1.0×10^{-17}
Capture cross section σ_e (σ_h) for valence band tail (cm ²)	1.0×10^{-15}	1.0×10^{-15}	1.0×10^{-14}	1.0×10^{-15}	1.0×10^{-15}
Gaussian density of states (cm ⁻³)	1.0×10^{17}	1.0×10^{16}	3.0×10^{17}	5.0×10^{15}	5×10^{18}
Gaussian peak energy for donor(acceptor) (eV)	1.5(0.98)	1.38(0.78)	1.22(0.70)	1.22(0.70)	1.22(0.70)
Standard deviation of Gaussian for donor (acceptor) (eV)	0.21(0.21)	0.21(0.21)	0.21(0.21)	0.21(0.21)	0.21(0.21)
Capture cross section σ_e (σ_h) for donor-like Gaussian States (cm ²)	1.0×10^{-14}	1.0×10^{-14}	1.0×10^{-13}	1.0×10^{-14}	1.0×10^{-14}
Capture cross section σ_e (σ_h) for acceptor-like Gaussian states (cm ²)	1.0×10^{-15}	1.0×10^{-15}	1.0×10^{-14}	1.0×10^{-15}	1.0×10^{-15}
	(1.0×10^{-14})	(1.0×10^{-14})	(1.0×10^{-13})	(1.0×10^{-17})	$1. \times 10^{-17}$

defective zone several nanometers thick with a short carrier lifetime is formed at the interface [12]. For simulation purposes, defect state for structure without buffer layer was achieved by inserting 2 nm (i)a-Si:H layer between (p)nc-Si:H/(i)a-Si:H as a defective layer with high density [23, 26].

Design parameters for optimization are shown in Table 1. Therefore, to investigate variations in efficiency, changes in V_{OC} , J_{SC} , and FF were determined in the dopant concentration of window layer (Na) and (n)a-Si:H layer (Nd). The absorber layer bandgap and the absorber layer thickness were validated with the spectral response of the solar cells and carried out by simulating the external quantum efficiency for wavelength ranging from 300 to 800 nm. The solar cell performances are described in several equations extracted from the J-V curve, including [27]

$$J_{SC} = J_L - J_0 \left(\exp \left(\frac{qV}{nKT} \right) - 1 \right) \quad (9)$$

$$V_{OC} = \frac{nKT}{q} \left(\ln \left(\frac{J_{SC}}{J_0} \right) + 1 \right) \quad (10)$$

$$E_{ff} = \frac{J_{SC} V_{OC} FF}{P_{in}} \quad (11)$$

$$FF = \frac{V_m J_m}{V_{OC} J_{SC}} = \frac{P_m}{V_{OC} J_{SC}} \quad (12)$$

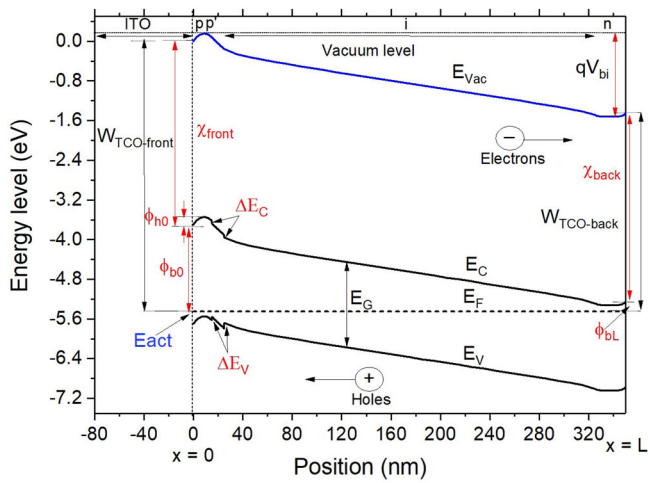
where J_{SC} is the current density at short circuit current, J_L is the photocurrent density, J_0 is the reverse dark current, V is thermal voltage over the junction, KT is the thermal energy, n is the ideality factor, V_{OC} is the open circuit voltage, V_m is the maximum voltage, J_m is the maximum current density, P_m is the maximum power, FF is fill factor, and E_{ff} is the conversion efficiency.

In this study, the influence of buffer layer performance analysis of the structures with and without buffer is expressed by the characteristics of the J-V curve under dark and illumination, with the quantum efficiency achieved through simulation with AFORS-HET software under AM1.5G spectral radiation with the power density of 100 mW/cm^2 as a light source. Simultaneously, the device's temperature is maintained at 300 K, with the light reflection at the front contact (RF) set to 0.2. Due to the absence of a back reflector in the simulation structures, the authors assumed that the back contact has a reflection coefficient (RB) of 0. The generation of e-h pairs for the optical model is obtained as outlined either by Lambert-Beer absorption, including rough surfaces and measured reflection and transmission, or by calculating the plain surface incoherent/coherent multiple internal reflections complex indices of reflection for the individual layers [28]. The DC mode was used to simulate pin and p-p'-i-n solar cells to represent steady-state conditions under an external applied voltage or current. In this mode, all-time derivatives vanished, thereby leading to a simplified differential equation system, which is then solved for time-independent and position-dependent functions. All parameters were used in the simulation adopted from various references, as shown in Table 1 [21,23,29].

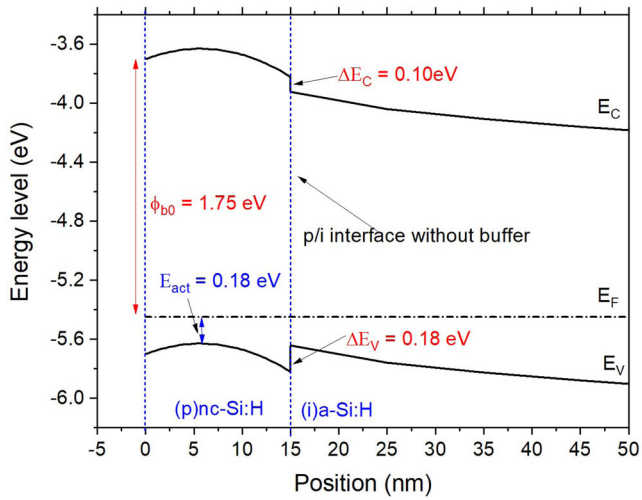
3. Simulation results and discussion

3.1. Simulated thermodynamics equilibrium bandgap diagram of the heterojunction solar cells

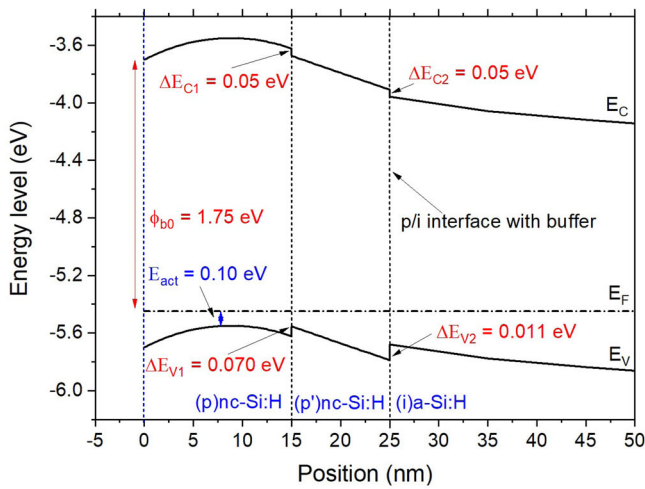
Fig. 2(a) displays the heterojunction solar cell structure's band diagram at thermodynamic equilibrium and calculated by an AFORS-HET simulator. The barrier heights (ϕ_{b0} and ϕ_{bL}) are related to the affinity of electron χ_e , the front and back contacts work functions ($W_{TCO-front}$ and $W_{TCO-back}$) with following expressions $\phi_{b0} = W_{TCO-front} - \chi_e /_{x=0}$ ($= 1.75 \text{ eV}$) and $\phi_{bL} = W_{TCO-back} - \chi_e /_{x=L}$ ($= 0.20 \text{ eV}$) [14]. Meanwhile, the values for the of $E_{ac}(p)$ and $E_{ac}(n)$ as activation energies are obtained as follows $E_{ac}(p) = \phi_{b0} - E_g(p) + \phi_h$, for front contact and the activation energy $\phi_{bL} = E_C - E_F = E_{ac}(n)$ for back contact. For solar cell cases with and without buffer, the barrier high for holes ϕ_h (surface band bending) for the p-layer in thermodynamics equilibrium depends on front contact TCO (ITO), the thickness of p-window layer, the concentration dopant, and density of states (DOS) [30]. From Fig. 2(b) and (c), the values of $\phi_h = \phi_{b0} - \phi_{b0}^n = 0$, which means that the p-layer in both structures gives an ohmic contact or does not band bending at TCO/p-layer interface [31]. For effective p-layer doping of $3 \times 10^{18} \text{ cm}^{-3}$, mobility band gap (E_g) 2.0 eV, and thickness of 15 nm, the barrier height is expressed as neutral barrier height $\phi_{b0}^n = \phi_{b0} - \phi_h = 1.75 \text{ eV}$ to hole movement.



(a)



(b)



(c)

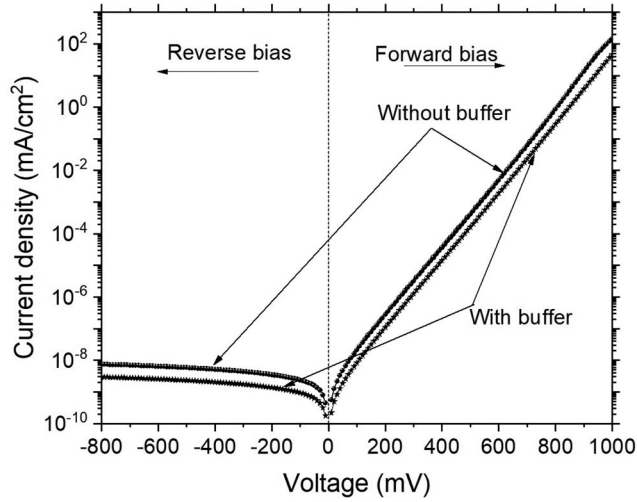
Figure 2. Simulated band diagrams of structures (a) in the entire device, (b) without buffer (p-i-n), (c) with buffer (p-p'-i-n) at thermodynamics equilibrium was generated using AFORS-HET simulator.

Whereas, the barrier height for the back contact, $\phi_{bL} = \phi_{bL}^n = 0.20 \text{ eV}$ was used to depict a neutral back contact.

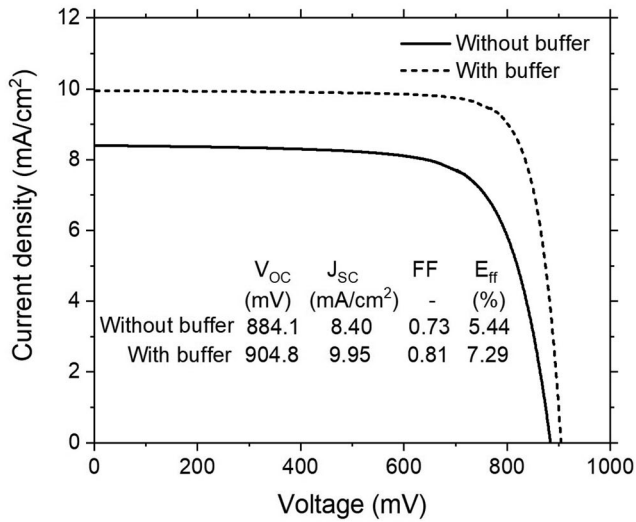
Fig. 2(b) displays p/i direct contact with 2 nm defective layer with defect density of approximately $3.0 \times 10^{17} \text{ cm}^{-3}$ which creates the conduction and valence band discontinuity (band offset) where $\Delta E_C = 100 \text{ meV}$ and $\Delta E_V = 180 \text{ meV}$, respectively. Meanwhile, by inserting the 10 nm of (p')nc-Si:H with light dopant concentration ($1.0 \times 10^{16} \text{ cm}^{-3}$) and defect density of $5.0 \times 10^{15} \text{ cm}^{-3}$ as buffer layer (Fig. 2(c)), the valence and conduction band offset values reduce to $\Delta E_V = 70 \text{ meV}$ and $\Delta E_C = 50 \text{ meV}$. This indicates reduced potential barrier height for collection of holes from active layer to window layer (p-layer), thereby increasing the series resistance diminished and charge collection properties are raised. The simulation results shows that the effect of the (p')nc-Si:H reduces valence band offsets. Furthermore, the conduction band offset (ΔE_C) remains constant with a large barrier blocking electron back diffusion and minimizing recombination in the front contacts. The valence band offset (ΔE_C and ΔE_V) reduction with insertion buffer layer and suitable bandgap, leads to an increase in built-in potential (V_{bi}) correlated with an enhanced V_{OC} [32].

3.2. The J-V characteristics (dark and illuminated) and EQE

Fig. 3(a) displays the dark J-V's simulated characteristics for solar cell structures with and without buffer using AFORS-HET. The characteristic of dark currents is a useful parameter in understanding the internal physical phenomena, which are the illuminated J-V characteristics of solar cells dependent on it. These dark current characteristics are used to estimate the mechanism of recombination process, the quality of junction, and contact resistance [33]. An explanation of Fig. 3(a) shows that by applying reverse bias (-900 – 0 mV), the dark currents for structures without buffer and with buffer obtained from simulation showed less significant discrepancy between the dark J-V characteristics and the two devices using current densities of 10^{-9} mA/cm^2 . The dark currents for structures with and without buffer layers are $3.27 \times 10^{-9} \text{ mA/cm}^2$ and $8.26 \times 10^{-9} \text{ mA/cm}^2$ at reverse bias of -900 mV. Meanwhile, the dark currents for both structures in the forward bias observed after 100 mV are influenced by buffer layer (p') at p/i interface and capable of decreasing the saturated current. This is based on the datum that in the forward bias of less than 250 mV, the dark current is strongly dependent to the recombination of the electron-hole pairs through the intermediate gap state in the intrinsic layer of the structure at forward bias of less than 100 mV. It becomes limited due to the combination of diffusion and recombination for region voltage between 100 and 250 mV, which is not influenced by the quality of the doped layers or the contacts [14, 34]. In the region of forward bias between 100 – 250 mV the solar cells for both structures enters into electron space charge limited current (SCLC) recombination near to the window-layer, where dark current tumbles and escalates slowly with the forward bias. At high forward bias values greater than 400 mV, the dark current entirely determined by hole injection at TCO/p-layer interface, electron-hole recombination in absorber layer, hole transport in buffer and window layers, electron transport across the n-layer/back contact interface, and electron drift over the absorber layer by SCLC [34].



(a)



(b)

Figure 3. Simulated the J-V characteristics (a) under dark (b) under illumination for solar cells without buffer and with buffer.

The simulated J-V characteristic under light for with and without buffer structures is shown Fig. 3(b). The results show that solar cells with buffer layer have better performance compared to those without buffer, as illustrated by higher J_{SC} and V_{OC} values, which significantly increase FF as well as conversion efficiency. After inserting the 10 nm (p')nc-Si:H between (p)nc-Si:H and (i)a-Si:H layers, the V_{OC} , J_{SC} , and FF increased by 20.7 mV, 1.55 mA/cm², and 0.08, thereby leading to a rise in conversion efficiency for structure with buffer layer by 2.01%. The calculations yielded a conversion efficiency value of 5.44% for solar cells without buffer layer ($V_{OC} = 884.1$ mV, $J_{SC} = 8.40$ mA/cm², $FF = 0.730$) and 7.29% for those with buffer cells ($V_{OC} = 904.8$ mV, $J_{SC} = 9.95$ mA/cm²,

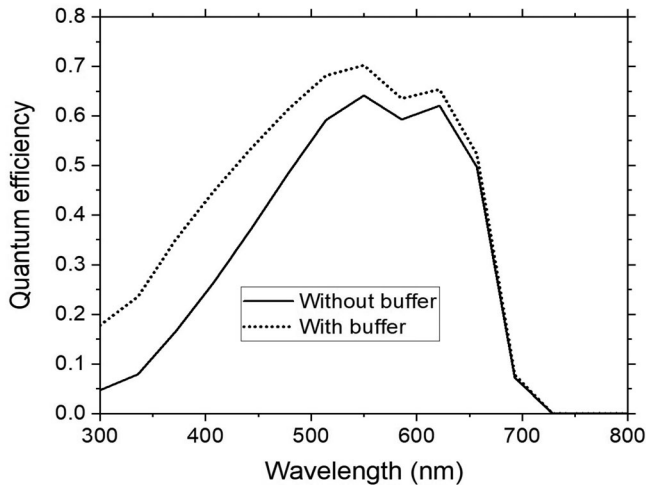


Figure 4. Simulated spectral response under illumination ($V=0V$) for solar cells without buffer and with buffer.

$FF=0.810$). Incorporation of (p')nc-Si:H as the buffer layer tends to reduce the defect rich region (DRR), which has a high defect density due to influential band bending at the front interface, thereby recombination rate is increase [7].

Fig. 4 shows the spectral response of the external quantum efficiency (QE) used to evaluate both structures' spectral response, which exhibits that a structure without buffer has a low response for the range of short-wavelength (blue region) due to high recombination at the p/i interface. Therefore, this led to a decrease in the J_{SC} , which was smaller than a structure with a buffer layer. The quantum efficiency of solar cells has a peak value of 70.20% (with buffer) and 64.17% (without buffer) at a 550 nm wavelength, respectively. Good response in the blue region indicates that the photo-generated charge carrier is efficiently extracted from the DRR at interface. The presence of a buffer layer on the solar cell structure increases the blue response's ability, which leads to a higher J_{SC} . Furthermore, the structure without buffer has a low blue spectral response due to high recombination at the heterojunction (p)nc-Si:H/(i)a-Si:H interface [35]. The external quantum efficiency (EQE) simulated results for both structures, indicates that the cell has an excellent spectral response in wavelength range of 300 nm to 657 nm.

3.3. Impact of the (p')nc-Si:H with respect to the p/i interface on solar cells performances

Therefore, the presence of (p')nc-Si:H layer reduces the valence and conduction band offsets at the p/i interface by avoiding holes that moves toward p-window layer from the absorber layer and which acts as a mirror for the electron [12]. The incorporation of a 2 nm a-Si:H acts as a defective region for structures without buffer layer to create (p)nc-Si:H/a-Si:H interface, which serves as a channel for the recombination and considerable trapping of holes [26].

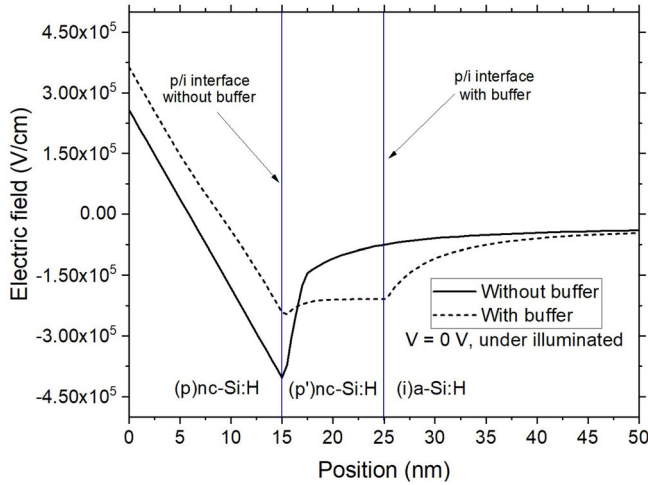
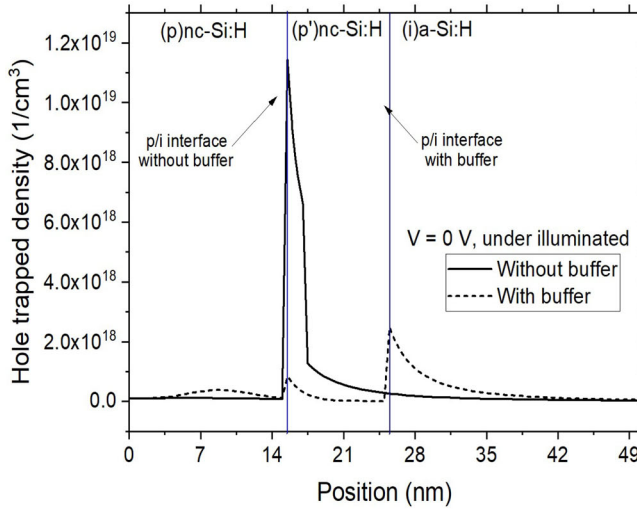


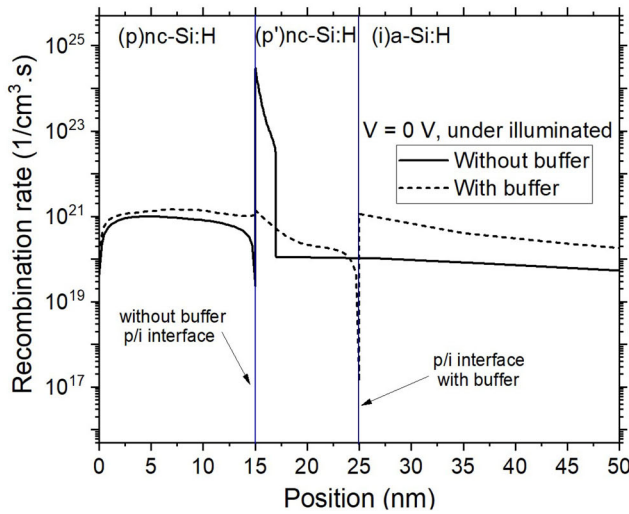
Figure 5. Distribution of Electric field as a function of distance at p/i interface under illumination ($V = 0$ V).

Fig. 5 shows the electric field distribution under illumination as a function of distance inside solar cells for both structures. The pin solar cell with and without buffer layers in short circuit current ($V = 0$ V) produced electric field at p/i interface, with maximum values of 2.42×10^5 Vcm^{-1} and 4.04×10^5 Vcm^{-1} . For a structure without buffer, the presence of the valence band offset caused the p/i interface layer traps to produce photogenerated holes, which leads to a large electric field. Furthermore, the potential goes down in active region due to the presence of the defective layer with the low values of V_{OC} and FF . Conversely, the electrical field within the buffer layer needs to be constant to maintain a higher absorber layer. However, the V_{OC} and FF values arise in the structure with buffer layer from the smallest potential drop over the p/i interface, thereby producing a high electrical field over absorber layer [9, 26]. The deposition process of solar cell fabrication with different conditions produces the bandgap mismatch at the interface, thereby leading to offset and charge extraction loss, especially at the p/i interface, which affects the performance of the devices [33].

As mentioned above, the formation of the valence band offset behaves like the center of the holes trapped for both structures, as depicted in Fig. 6(a). For structures without buffer, the trapped holes density interface was observed 1.14×10^{19} cm^{-3} . Meanwhile, for those with buffer the trapped holes density decreased due to presence of buffer layer at 8.42×10^{17} cm^{-3} . Fig. 6(b) shows a comparison of the total recombination rate at p/i interface region between structures with and without buffers. In this case, the structure with buffer layer has less total recombination rate of about 1.39×10^{17} $\text{cm}^{-3} \cdot \text{s}^{-1}$ be stack up to the structure without buffer of approximately 2.99×10^{24} $\text{cm}^{-3} \cdot \text{s}^{-1}$, which is calculated under illumination condition at $V = 0$ V. This is due to the high electrical field strength in front, generates many carriers close to this place. The recombination rate losses at the p/i region affect the V_{OC} , which remains high as a higher electrical field in this region reduces the average carrier transit time over DRR at the p/i region [7].



(a)



(b)

Figure 6. (a) The holes trapped density (b) the total carrier recombination as a function of distance at p/i interface under illumination ($V = 0$ V).

3.4. Optimization of the dopant concentration (N_a and N_d) heterojunction solar cells

In this section, the authors focused on enhancing the performances for structure with buffer (p-p'-i-n) by optimizing the p-layer dopant concentration (N_a) and the n-layer dopant concentration (N_d). The p-window and n-layers optimization process was carried out by reviewing the effect of changes in acceptor and donor concentration on the performance of the solar cell expressed by the open circuit voltage (V_{OC}), the short circuit current (J_{SC}), the fill factor (FF) and the efficiency (E_{ff}) with all input parameters

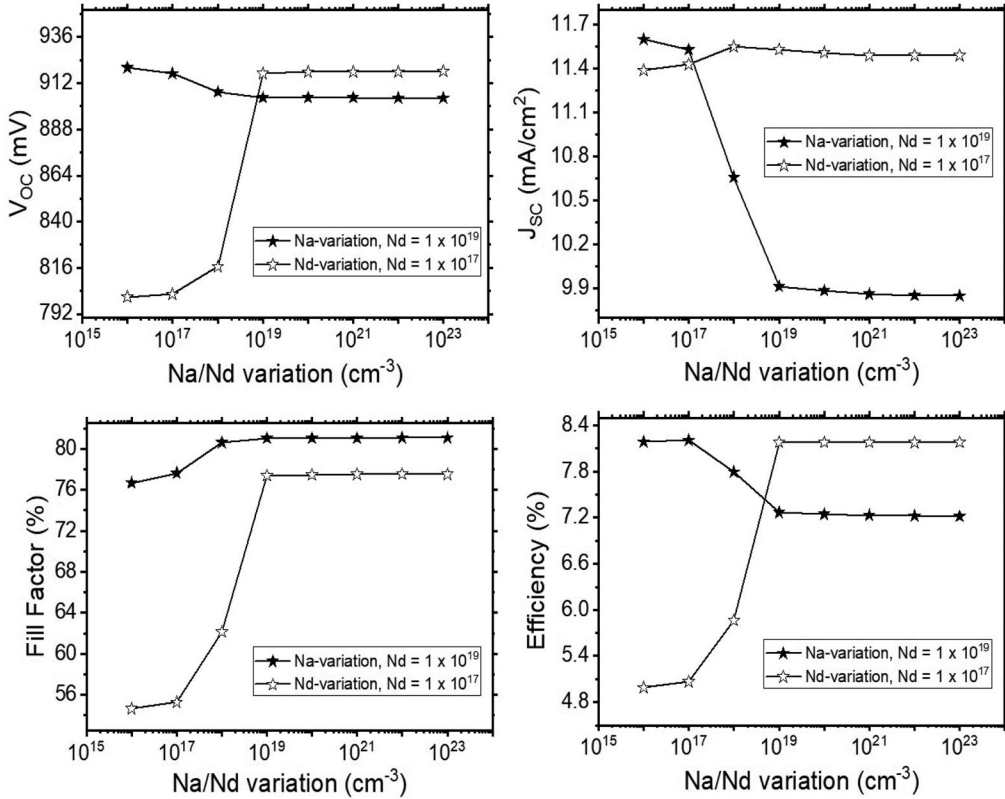


Figure 7. Simulated results of (a) the open circuit voltage (b) the short circuit current, (c) the fill factor, and (d) the efficiency of the p-p'-i-n solar cell with Na and Nd of the p and n layers for structure with buffer (p-p'-i-n).

kept constant, as shown in Table 1. During the simulation process, the Na dopant concentration value of the p-window layer and Nd concentration of n-layer varied from 1.0×10^{16} to 1.0×10^{23} particles/cm³ with the work function of the TCO/(p)nc-Si:H contact is a flat-band. This is similar with the distribution of the gap states in a-Si:H and (p')nc-Si:H/(i)a-Si:H interface, which causes a pinning effect to limit the movement of E_F in (n)a-Si:H layer [23]. Additionally, the thickness and bandgap are kept constant at 15 nm, 2.0 eV (for the p-window layer), and 25 nm, 1.72 eV (for the n-layer). The effect of doping variations on V_{OC} , J_{SC} , FF , and E_{ff} parameters for a structure with buffer are shown in Fig. 7(a)-(d).

Fig 7(a) shows that V_{OC} is declines from 920.1 mV to 904.6 mV with an increase in Na dopant concentration from 1.0×10^{16} to 1.0×10^{19} particles/cm³ before saturation. An increase in the Na doping concentration, V_{OC} enhances the larger quasi-Fermi energy-level splitting at higher bandgap ($E_g = 2.0$ eV for p-window layer), thereby leading to a rise in TCO/p interface by the type-p layer [36]. Meanwhile, the V_{OC} increases from 800.9 mV to 917.9 mV with a rise in Nd dopant concentration from 1.0×10^{16} to 1.0×10^{20} particles/cm³ with constant values of N_A dopant concentration at 1.0×10^{17} particles/cm³. The V_{OC} is associated with the -p and -n layers dopant concentration

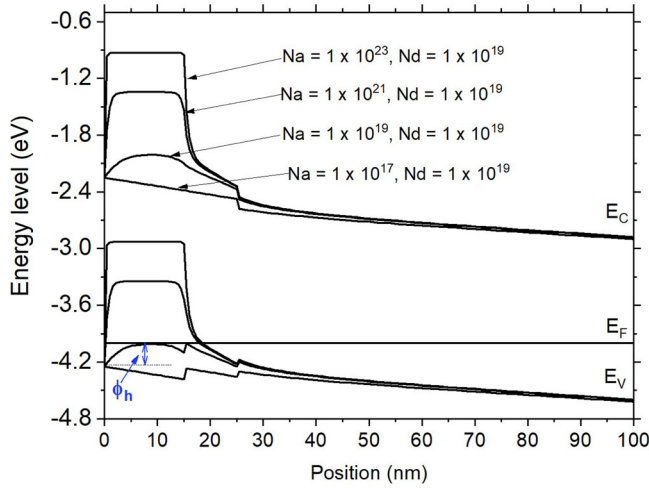


Figure 8. Simulated band diagram of the p-p'-i-n solar cell at certain N_a dopant concentration for N_d dopant concentration 1.0×10^{19} particles/cm³.

through the photovoltage process to increased built-in potential (V_{bi}), which described by the following expression [24]

$$V_{bi}(p - p' - n) = V_{OC}(p - p') - V_{OC}(p' - n) = \frac{KT}{q} \ln\left(\frac{N_A N_D}{n_i^2}\right) \quad (13)$$

where K , T , q , N_A , N_D , and n_i are the Boltzmann constant, temperature, unit charge, dopant concentration in p-window layer, dopant concentration in n-layer, and concentration of the intrinsic carrier, respectively.

According to Figs. 2 and 8, the relationship between open-circuit voltage (V_{OC}) and the effective built-in potential (V_{bi}) is described as follows [14]

$$V_{OC} = \frac{1}{q} \left[V_{bi} - nKT \ln\left(\frac{qN_V S_{it}}{J_{SC}}\right) \right] \quad (14)$$

$$V_{bi} = W_{front-TCO} - \chi_e /_{x=0} - \phi_{bL} \quad (15)$$

where n , KT , N_V , S_{it} , $W_{front-TCO}$, $\chi_e /_{x=0}$, ϕ_{bL} are the factor of diode ideality, the thermal energy, the density of states in the valence band, the velocity of interface recombination, the work function at the front, the affinity of electron of p-window layer, and the barrier height at back contact, respectively. It indicates that an increase in dopant concentration leads to a rise in V_{bi} and V_{OC} .

Fig. 7(b) displays the value of J_{SC} decreased continuously from 11.6 to 9.85 mA/cm², which is in accordance with a rise in N_a from 1.0×10^{16} to 1.0×10^{23} particles/cm³. Fig. 8 shows that the change in the surface band bending (ϕ_h) quantity present a barrier height with a photogenerated hole that exists from the cell when doping concentration of p-window layer changes, with the majority of the carrier collected at the front contact. The fill factor increased from 0.767 to 0.811 with a rise in the p-layer dopant from 1.0×10^{16} to 1.0×10^{22} cm⁻³ and remains constant. Meanwhile, the fill factor (FF) increased from 0.547 to 0.775 with a rise in doping concentration of the n-layer (N_D)

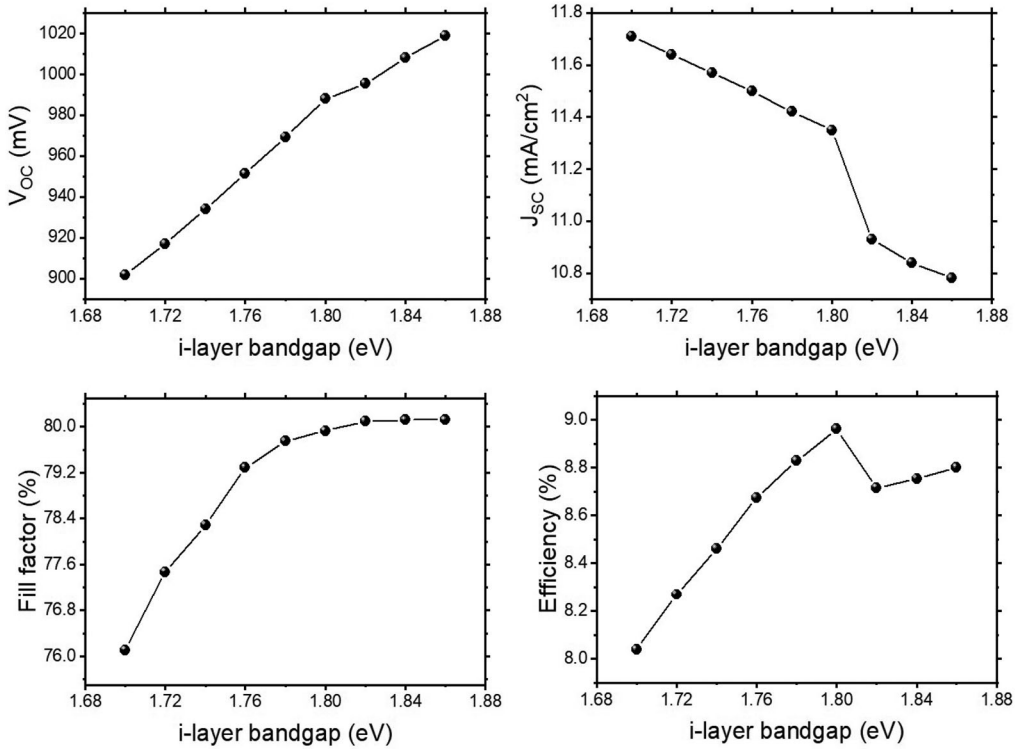


Figure 9. Simulated results of (a) the open circuit voltage (b) the short circuit current, (c) the fill factor, and (d) the efficiency of the p-p'-i-n solar cell with changes of the absorber layer.

from 1.0×10^{16} to $1.0 \times 10^{23} \text{ cm}^{-3}$, as depicted in Fig. 7(c). The improvement of conversion efficiency (E_{ff}) from 8.18% is achieved when the dopant concentrations of the p-window and the n-layers are 1.0×10^{17} particles/cm³ and 1.0×10^{19} particles/cm³, respectively, as shown in Fig. 7(d).

3.5. The bandgap and thickness optimization of the absorber layer heterojunction solar cells

The intrinsic layer absorbs photon through the p-window and the created hole-electron pairs. In simulation, the bandgap value 2.0 eV for window layer, 1.88 eV for buffer layer, and 1.72 eV for absorber and n-layers. In addition, their thickness was 15 nm, 10 nm, 300 nm, and 25 nm, respectively. Fig. 9(a)–(d) displays the values of the open circuit voltage (b) the short circuit current, (c) the fill factor, and (d) the efficiency of the p-p'-i-n solar cell with changes of the absorber layer band gap associated with the absorber layer bandgap. As depicted in Fig. 9(a), the V_{OC} is increased gradually from 902 to 1019 mV with increasing the absorber layer bandgap from 1.7 to 1.86 eV associated with enhancement built-in potential across absorber layer as shown in equation (11). In contrast, J_{SC} decreased slowly from 11.71 to 11.35 mA/cm², while increasing the absorber bandgap from 1.70 to 1.80 eV, before it drastically decreased to 10.78 mA/cm² when the absorber layer bandgap was 1.86 eV, as depicted in Fig. 9(b). The reduction in J_{SC} with an increase in the absorber layer bandgap was based on an interaction between photon

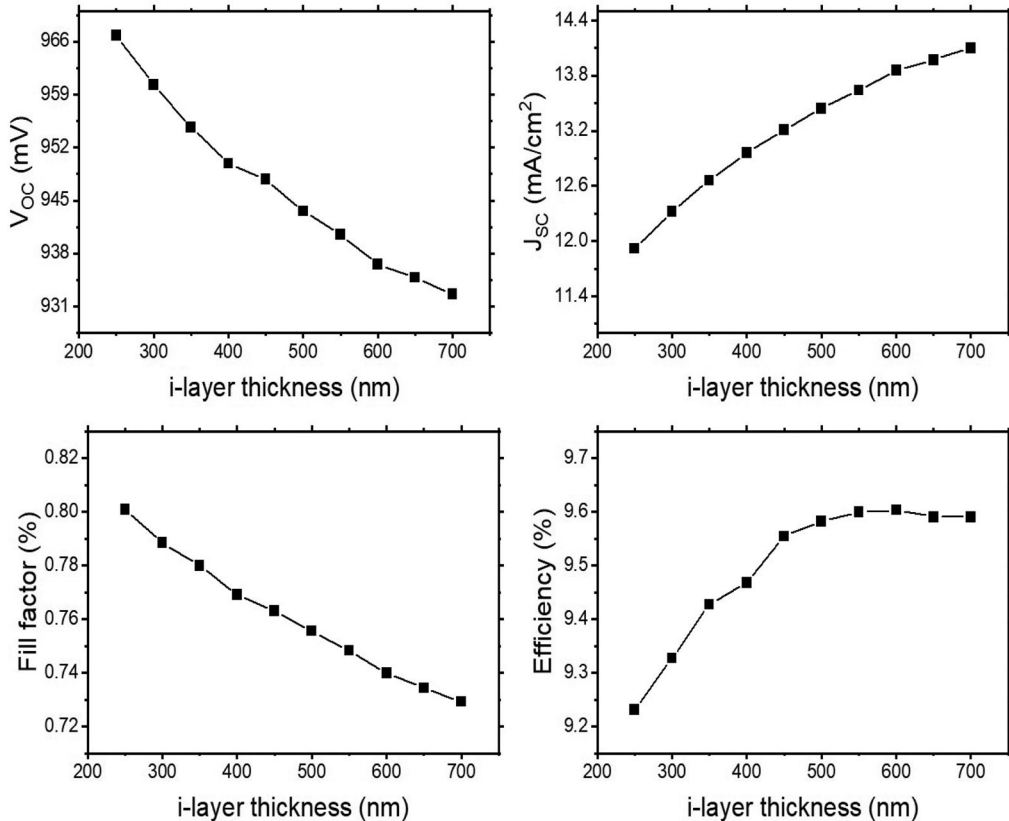


Figure 10. Simulated results of (a) the open circuit voltage (b) the short circuit current, (c) the fill factor, and (d) the efficiency of the p-p'-i-n solar cell with changes of the absorber thickness.

energy ($h\nu$) and material bandgap (E_g) with three possibilities, namely (i) $h\nu < E_g$ (no photons are absorbed), (ii) $h\nu = E_g$ (all photon were absorbed leading to maximum e-h pairs), and (iii) $h\nu > E_g$ (photon which absorbed have energy higher than E_g which due to heat loss) [14, 36]. Therefore, for photons with energy less or higher than bandgap, the absorber layer produces less e-h, thereby reducing J_{SC} . Fig. 9(c) displays the variation of fill factor (FF) respect to the absorber layer bandgap with an increase in trend from 0.761 to 0.801 for changes of bandgap between 1.70 to 1.82 eV, after that FF terraces to 0.812 for bandgap beyond 1.82 eV. However, the solar cells efficiency showed in Fig. 9(d) increased from 8.04% to 8.96% with a rise in the absorber bandgap from 1.70 to 1.80 eV. However, beyond 1.80 eV, the value of E_{ff} was found decreased. Furthermore, a maximum value of 8.96% is obtained when bandgap is at 1.80 eV, which increases the efficiency of solar cells. Therefore, the absorber bandgap is 1.8 eV was optimized.

The absorber layer thickness optimization for the p-p'-i-n solar cells conducted by the dopant concentration of the window, buffer, and n-layers were 1.0×10^{17} , 1.0×10^{16} , and 1×10^{19} particles/cm³, respectively. Meanwhile, optimized band gap values for the window layer, buffer, absorber, and n-layers were 2.0 eV, 1.88 eV, 1.80 eV, and 1.72 eV, respectively. However, the thickness of the window, buffer, and n-layers

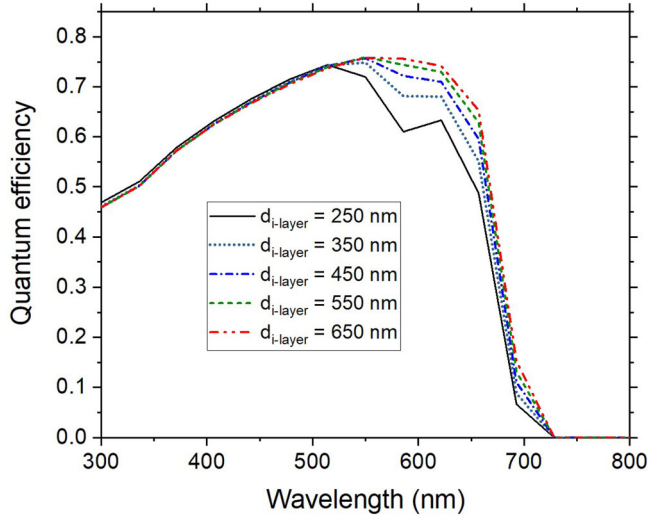


Figure 11. Simulated quantum efficiency of the p-p'-i-n solar cell with changes of the absorber thickness.

was kept constant at 15 nm, 10 nm, and 25 nm. Fig. 10(a)–(d) displays the external parameter variation of V_{OC} , J_{SC} , FF , and E_{ff} with respect to absorber thickness comprising of a buffer (p-p'-i-n). Fig. 10(a) displays the V_{OC} declined with an increase in thickness value of the absorber layer from 250 nm ($V_{OC} = 966.8$ mV) to 700 nm ($V_{OC} = 932.6$ mV). In other words, the V_{OC} subsides by 34.2 mV when the absorber layer thickness escalates from 250 to 700 nm. This proves that V_{OC} does not hinge on the thickness of the absorber, rather it depends on the properties of the doped layer and the recombination rate at p/i region [14]. Fig. 10(b) illustrates variation of J_{SC} with changes of the absorber thickness, where J_{SC} was continuously terraced from 11.92 to 14.10 mA/cm² when absorber thickness is changes from 250 to 700 nm due to larger in photon absorption as depicted in Fig. 11. However, the variation of FF respect to absorber thickness gradually decreased from 0.801 to 0.729 due to the internal electric field across absorber layer is lower (Fig. 5) as depicted in Fig. 10(c). The variation of conversion efficiency (E_{ff}) ranges from 9.23% to 9.60% in values of 250 to 600 nm and declined with an increase in the absorber layer thickness (Fig. 10 (d)). Finally, to obtain better solar cell efficiency, the absorber layer thickness of 600 nm is optimized.

Fig. 11 displays the quantum efficiency (QE) of the p-p'-i-n solar cell when the absorber thickness from 250 to 700 nm more e-h pairs is generated by photon wavelength from 300 to 520 nm. The quantum efficiency is enhanced in this range of the spectrum (blue region), as followed in equations (16) and (17). Consequently, the J_{SC} is increased for photon wavelength from 520 to 630 nm, after that the QE decreases for all the absorber thickness and the J_{SC} reduces. The J_{SC} is calculated by integrating the external quantum efficiency (EQE) spectrum for the solar cell under standard AM1.5G illumination as expressed by [37].

$$J_{SC} = \int_{300 \text{ nm}}^{800 \text{ nm}} \left[\frac{q\lambda}{hc} \phi_{AM1.5}(\lambda) EQE(\lambda) \right] d\lambda \quad (16)$$

Table 2. Two Simulated results of the p-p'-i-n solar cell using AFORS-HET simulator are compared with AMPS-1D [14].

References	WF _{ITO} (eV)	E _{g,i-layer} (eV)	d _{i-layer} (nm)	V _{OC} (mV)	J _{SC} (mA/cm ²)	FF	E _{ff} (%)
Belfar (2015)	5.45	1.78	550	936.0	13.96	0.714	9.35
This work	5.45	1.80	600	936.6	13.86	0.738	9.60

$$EQE(\lambda) = \frac{J_{SC}(\lambda)}{q\Phi(\lambda)} = \frac{J_{SC}}{q} \left(\frac{hv}{P_{Opt}} \right) \quad (17)$$

where h is Plank's constant, c is the speed of light, q is the unit charge, $\phi_{AM1.5}$ is the solar spectral irradiance under air mass 1.5 G, $\Phi(\lambda)$ is the photon flux, and P_{opt} is the optical power, respectively.

Table 2 displays the optimization results of p-p'-i-n heterojunction solar cell using AFORS-HET simulator are compared with optimization using AMPS-1D for n-i-p'-p solar cell was carried out by Belfar, 2015 [14].

4. Conclusion

This research utilized the AFORS-HET to simulate pin-type a-Si:H/nc-Si:H heterojunction solar cell by involving the (p')nc-Si: H bilayer, which acts as a p-window and buffer layer. Firstly, the authors' simulated band diagrams of structures with and without buffer at thermodynamics equilibrium to determine the dark and illuminated J-V characteristics, and the external quantum efficiency (EQE) needed to observe the effects of the presence of a buffer layer to changes of potential barrier height at front contacts, to narrow the band offset at the p/i interface region, elevates the distribution of electric field, minimize the density of trapped holes, and mitigate the total recombination rate at the p/i interface region. Secondly, in an effort to enhances the electrical and the optical properties of p-p'-i-n heterojunction solar cell, each layer was optimized including dopant concentration for the p-window and n-layers, the absorber band gap, and its thickness, respectively. During simulation, the N_a and N_d dopant concentrations, the absorber layer band gap, and its thickness varied from 1.0×10^{16} to 1.0×10^{23} particles/cm³, 1.7 to 1.86 eV, and 250 to 700 nm. The simulation results indicated that the efficiency of p-p'-i-n solar cell is enhanced by 7.29% ($V_{OC} = 904.8$ mV, $J_{SC} = 9.95$ mA/cm², $FF = 0.810$) to 9.60% ($V_{OC} = 936.6$ mV, $J_{SC} = 13.86$ mA/cm², $FF = 0.738$) and optimized when values of the N_A , N_D , absorber layer band gap, and thickness parameters are 1.0×10^{17} particles/cm³, 1.0×10^{19} particles/cm³, 1.80 eV, and 600 nm, respectively. Finally, the results were compared using AMPS-1D simulator as shown in Table 2. The proposed structure of p-p'-i-n heterojunction solar cell provide a reference for further development of low cost and efficient in solar cell technology.

Acknowledgments

The authors are also grateful to HZB for the AFORS-HET Simulation Program.

Funding

The authors are grateful to BUDI-LPDP Kementerian Keuangan RI for providing the financial grant needed to carry out this research (Grant number: PRJ-5441/LPDP.3/2016).

ORCID

Dadan Hamdani  <http://orcid.org/0000-0002-5370-0559>

Gatut Yudoyono  <http://orcid.org/0000-0003-1115-1560>

Darminto Darminto  <http://orcid.org/0000-0002-6269-9246>

References

- [1] V. V. Tyagi *et al.*, *Renewable Sustainable Energy Rev.* **20**, 443 (2013). doi:10.1016/j.rser.2012.09.028
- [2] W. Qarony *et al.*, *Results Phys.* **7**, 4287 (2017). doi:10.1016/j.rinp.2017.09.030[]
- [3] M. Riaz *et al.*, *Opt. Express* **26**, A626-A635 (2018). doi:10.1364/OE.26.00A626
- [4] W. H. Son *et al.*, *Mol. Crystals Liquid Crystals* **676** (1), 131 (2018). doi:10.1080/15421406.2019.1596229
- [5] M. Green *et al.*, *Prog. Photovolt. Res. Appl.* **29** (1), 3 (2021). doi:10.1002/pip.3371
- [6] H. Mehmood, and T. Tauqeer, *IET Circuits, Dev. Syst.* **11** (6), 666 (2017). doi:10.1049/iet-cds.2017.0072
- [7] G. Ahmad *et al.*, *IEEE J. Photovoltaics* **7** (2), 414 (2017). doi:10.1109/JPHOTOV.2016.2642644
- [8] G. Das *et al.*, *Mater. Sci. Semicond. Process.* **24**, 50 (2014). doi:10.1016/j.mssp.2014.03.009
- [9] B. Rech, C. Beneking, and H. Wagner, *Sol. Energy Mater. Sol. Cells* **41-42**, 475 (1996). doi:10.1016/0927-0248(95)00127-1
- [10] S. Guha *et al.*, *Appl. Phys. Lett.* **49** (4), 218 (1986). doi:10.1063/1.97176
- [11] K. Tao *et al.*, 4th IEEE International Conference on Nano/Micro Engineered and Molecular Systems, pp. 327–330, 2009.
- [12] J. Park *et al.*, *Thin Solid Films* **546**, 331 (2013). doi:10.1016/j.tsf.2013.06.064
- [13] M. I. Kabir *et al.*, *International Journal of Photoenergy* **2012**, 1 (2012). doi:10.1155/2012/460919
- [14] A. Belfar, *Sol. Energy* **114**, 408 (2015). doi:10.1016/j.solener.2015.02.010
- [15] L. Bechane, N. Bouarissa, and K. Loucif, *Trans. Electr. Electron. Mater.* (2020). doi:10.1007/s42341-020-00262-4
- [16] R. Varache *et al.*, *Sol. Energy Mater. Sol. Cells* **141**, 14 (2015). doi:10.1016/j.solmat.2015.05.014
- [17] V. Kanneboina, *J. Comput. Electron.* **20**, 344 (2021).
- [18] S. M. Iftiqar *et al.*, *Sol. Energy Mater. Sol. Cells* **204**, 110238 (2020). doi:10.1016/j.solmat.2019.110238
- [19] P. Procel *et al.*, *Sol. Energy Mater. Sol. Cells* **186**, 66 (2018). doi:10.1016/j.solmat.2018.06.021
- [20] J. A. Davis *et al.*, *Front. Phys.* **8**, 158, (2020). doi:10.3389/fphy.2020.00158
- [21] N. Hernández-Como, and A. Morales-Acevedo, *Sol. Energy Mater. Sol. Cells* **94** (1), 62 (2010). doi:10.1016/j.solmat.2009.05.021
- [22] I. Benigno, and D. Darminto, *IJOS.* **2** (3), 37 (2017). doi:10.12962/j23378530.v2i3.a3184
- [23] A. Belfar, and H. Ait-Kaci, *Thin Solid Films* **525**, 167 (2012). doi:10.1016/j.tsf.2012.10.060
- [24] A. Lin *et al.*, *J. Semicond.* **33** (2), 023002 (2012). doi:10.1088/1674-4926/33/2/023002
- [25] A. Froitzheim *et al.*, Proceedings of 3rd World Conference on Photovoltaic Energy Conversion, 2003, pp. 279–282. Vol. 1, (2003).
- [26] N. Palit, and P. Chatterjee, *J. Appl. Phys.* **86** (12), 6879 (1999). doi:10.1063/1.371767
- [27] L. Chen *et al.*, *J. Semicond.* **38** (5), 054005 (2017). doi:10.1088/1674-4926/38/5/054005

- [28] L. Zhao *et al.*, *Sol. Energy Mater. Sol. Cells* **92** (6), 673 (2008). doi:[10.1016/j.solmat.2008.01.018](https://doi.org/10.1016/j.solmat.2008.01.018)
- [29] S. Singh, S. Kumar, and N. Dwivedi, *Sol. Energy* **86** (5), 1470 (2012). doi:[10.1016/j.solener.2012.02.007](https://doi.org/10.1016/j.solener.2012.02.007)
- [30] F. A. Rubinelli, J. K. Arch, and S. J. Fonash, *J. Appl. Phys.* **72** (4), 1621 (1992). doi:[10.1063/1.351679](https://doi.org/10.1063/1.351679)
- [31] A. Belfar, and H. Aït-Kaci, *Mater. Sci. Eng.: B* **178** (7), 438 (2013). doi:[10.1016/j.mseb.2013.01.018](https://doi.org/10.1016/j.mseb.2013.01.018)
- [32] J. Fang *et al.*, *Sol. Energy Mater. Sol. Cells* **128**, 394 (2014). doi:[10.1016/j.solmat.2014.06.012](https://doi.org/10.1016/j.solmat.2014.06.012)
- [33] G. Ahmad, G. Das, and J. N. Roy, *J. Mater. Sci: Mater. Electron.* **30** (13), 12406 (2019). doi:[10.1007/s10854-019-01599-0](https://doi.org/10.1007/s10854-019-01599-0)
- [34] A. Sturiale *et al.*, *J. Appl. Phys.* **106** (1), 014502 (2009). doi:[10.1063/1.3151691](https://doi.org/10.1063/1.3151691)
- [35] Y. Vygranenko *et al.*, *Sol. Energy Mater. Sol. Cells* **94** (11), 1860 (2010). doi:[10.1016/j.solmat.2010.06.044](https://doi.org/10.1016/j.solmat.2010.06.044)
- [36] M. Sharma *et al.*, *Silicon* **9** (1), 59 (2017). doi:[10.1007/s12633-015-9331-6](https://doi.org/10.1007/s12633-015-9331-6)
- [37] L. Hao *et al.*, *J. Elec. Mater.* **48** (7), 4688 (2019). doi:[10.1007/s11664-019-07241-3](https://doi.org/10.1007/s11664-019-07241-3)